Aerosol Science and Technology 36: 617–631 (2002)

Published by Taylor and Francis
0278-6826/02/$12.00 + .00

A Numerical Characterization of Particle Beam Collimation by an Aerodynamic Lens-Nozzle System: Part I. An Individual Lens or Nozzle

Xuefeng Zhang,[1] Kenneth A. Smith,[1] Douglas R. Worsnop,[2] Jose Jimenez,[2] John T. Jayne,[2] and Charles E. Kolb[2]
[1]*Department of Chemical Engineering, Massachusetts Institute of Technology, Cambridge, Massachusetts*
[2]*Center for Aerosol and Cloud Chemistry, Aerodyne Research, Inc, Billerica, Massachusetts*

Particle beams have traditionally been produced by supersonic expansion of a particle-laden gas through a single nozzle to vacuum. However, it has been shown that, by passing the particle-laden gas through a series of axi-symmetric subsonic contractions and expansions (an aerodynamic lens system) prior to the supersonic expansion to vacuum through a single nozzle, beam divergence can be significantly reduced. In this paper, particle motion in expansions of a gas-particle suspension through either a single lens or a single nozzle have been investigated numerically. Since the single aerodynamic lens and the isolated nozzle are the elementary components of any aerodynamic lens-nozzle inlet system, a fundamental understanding of these components is essential for designing an inlet system with the desired sampling rate, collimation, and transmission properties. If a gas undergoes subsonic contraction and expansion through an orifice, the associated particles would follow the fluid streamlines if the particles were inertialess. However, real particles may either experience a displacement toward the axis of symmetry or may impact on the front surface of the lens. The first of these effects leads to collimation of the particles near the axis, but the second effect leads to particle loss. It is found that the maximum particle displacement occurs at a particle Stokes number, St, near unity and significant impact loss also begins at St $\cong$ 1. The lens dimensionless geometry and the Reynolds number of the flow are other important parameters. When a gas containing suspended particles undergoes supersonic expansion through a nozzle to vacuum from the lens working pressure (~ 300 Pa), it is found that particle beam divergence is a function of Reynolds number, nozzle geometry, and particle Stokes number. More specifically, it is found that a stepped nozzle generally helps to reduce beam divergence and that particle velocity scales with the speed of sound.

INTRODUCTION

Particle beams have been used extensively in aerosol measurements since they were first produced by Murphy and Sears (1964). Interest accelerated in the last decade because collimated particle beams have facilitated online measurements of the size and chemical composition of individual particles (e.g., Davis 1977; Johnston and Wexler 1995; Murphy and Thomson 1995; Noble and Prather 1996; Jayne et al. 2000; and Tobias et al. 2000). Such measurements are essential to a determination of the origin of atmospheric particles and their impact on public health (Henry 1998).

Almost all online particle sizing and chemical analysis techniques employ particle beams of controlled dimensions and divergences. In these techniques, the particle beam is generated by expanding a gas-particle suspension through single or multiple orifices. Typically, particle time-of-flight (TOF) over a certain distance is measured by light scattering to determine particle terminal velocity, from which particle size can be inferred. The particles are either subsequently ablated by a laser beam followed by TOF mass spectrometric analysis (Murphy and Thompson 1995; Noble and Prather 1996) or are evaporated on a hot surface followed by electron impact ionization and quadrupole mass spectrometric analysis (Davis 1977; Jayne et al. 2000; Tobias et al. 2000). Recent work of Jayne et al. (2000) has demonstrated the ability to ascertain molecular composition of size-resolved particles by using a chopped particle beam followed by mass spectrometric analysis. All of these measurements require highly collimated particle beams, especially for the laser-based techniques because the laser beams are highly focused (~0.5 mm in diameter, Mallina et al. (2000) Thomson et al. (1997)). Ideally, the particle beam should be fully located within the laser beam.

Both theoretical and experimental approaches have been used to investigate the factors that control beam diameter and divergence. Traditionally, the particle beam was generated by expanding a gas-particle suspension from atmospheric pressure to vacuum through a single orifice, a method similar to that used in

---

Received 15 January 2001; accepted 23 May 2001.
This work was supported by EPA grant 82539-01-1.
Address correspondence to Kenneth A. Smith, Department of Chemical Engineering, Massachusetts Institute of Technology, Cambridge, MA 02139-4307. E-mail: kas@eagle.mit.edu

generating supersonic molecular beams (Kantrowitz and Grey 1951). Considerable measurement and modeling effort has been directed at providing quantitative information and fundamental understanding of the properties of such particle beams. Israel and Friedlander (1967) generated a particle beam with a divergence angle of 0.0055 rad for the 126–365 nm particle size range using capillaries and a low pressure source (~100 torr). Note that the value of the beam divergence angle here is defined as the beam radius at a certain distance from the nozzle exit divided by the distance. Estes et al. (1983) characterized capillary-generated particle beams and found that the beam was generally highly divergent (>0.02 rad divergence angle), except in a narrow range of particle diameters around 0.5 micron, for which the divergence angle was 0.005 rad. Dahneke and Cheng (1979a,b) calculated performance characteristics of particle beams generated by conically convergent nozzles and found that if a detector collects particles within a 1° (0.017 rad) divergence angle, it will detect 0.5–1 micron particles with 100% efficiency. Recent modeling results by Mallina et al. (1999) for conically convergent nozzles and for capillaries also found that only those particles within a narrow size range (referred to as the maximal collimation diameter) are efficiently collimated and, even for those maximally collimated particles, the divergence angle was on the order of 0.008 rad. If one considers the maximum beam divergence acceptable for current particle measuring instruments, these single nozzle systems are not adequate. For example, if one considers a sampling angle of 0.005 rad, which represents a 2.4 mm diameter resistance-heated particle vaporizer located 240 mm downstream, dimensions similar to that used by Jayne et al. (2000), the above data suggest that the single nozzle systems rarely provide 100% collection efficiency even at the maximum collimation particle diameter. For those systems employing laser beams as size detectors or ionization sources, the sampling efficiency is expected to be much lower as the laser beams are generally focused to a diameter of ~0.5 mm.

To reduce beam divergence, sheath flow has been used to confine the particles to a region close to the axis prior to the expansion through a single orifice/nozzle to vacuum. Dahneke and Cheng (1979b) investigated the effect of sheath flow on particle beam divergence and found that beam divergence angles can be reduced by a factor of 5 for 0.5 and 1.19 micron diameter polystyrene particles if 99% sheath flow is employed. Rao et al. (1993) and Kievit et al. (1996) also found that sheath flow improves beam quality. However, sheath flow also has some drawbacks, such as reducing particle sampling rate and difficulty in handling sheath gas, as pointed out by Liu et al. (1995a, b) and Kievit et al. (1996). Although it was proposed by Dahneke and Flachsbart (1972) in the early 1970s, it is no surprise that sheath flow technology has rarely been used in the practical particle analyses cited above. Alternatively, Liu et al. (1995a, b) centralized particles to a region close to the axis by forcing the gas-particle suspension to flow through a series of orifices (referred to as an aerodynamic lens system) prior to expanding the gas to vacuum through a final nozzle. It was found that the aerodynamic lens system provides the same function as the sheath flow without reducing the particle sampling rate or creating complications in gas handling. The pioneering work by Liu et al. (1995a, b) and recent characterizations by Jayne et al. (2000) have demonstrated that the technology significantly reduces beam divergence. The work of Schreiner et al. (1998, 1999) has extended the application of aerodynamic lenses to contexts in which the ambient pressure is low, such as in stratospheric research.

The aerodynamic lens-nozzle system proposed by Liu et al. (1995a, b) is shown schematically in Figure 1, which illustrates how such a series of individual lenses can be used to effectively transport particles into vacuum. The particle trajectories through the lens are calculated by Fluent (described later) for 500 nm diameter spheres, which have a density of 1000 kg/m^3. Except for the trace closest to the axis, each line in the figure represents the boundary of a region enclosing 10% of the particle flow rate. The calculation assumes that the particles are dispersed uniformly in the upstream gas and that the upstream gas velocity profile is parabolic. A 2.4 mm diameter target (detector) is located 240 mm downstream, and this configuration defines a sampling angle of 5×10^{-3} rad. Note that $X = 0$ is placed at the nozzle exit for this particular figure. One can see that the beam is highly collimated with a divergence angle of about 10^{-3} rad so that the collection efficiency on the target is 100%. The first 5 thin cylindrical orifices serve to collimate the particles onto the centerline; the final exit orifice generates a supersonic gas expansion governing particle acceleration into the vacuum system. During the final expansion, particles acquire a distribution of terminal velocities that depends on particle diameter, with smaller diameter particles accelerating to faster velocities and larger diameter particles accelerating to slower velocities. Measurement of this particle terminal velocity allows instruments equipped with aerodynamic lens systems to determine particle aerodynamic diameter.

Liu et al. (1995a, b) analyzed, both theoretically and experimentally, the particle beams produced by an aerodynamic lens-nozzle expansion. In their calculations, flow fields in the aerodynamic lenses were assumed to be incompressible or isentropic, whereas the supersonic free-jet expansion though the nozzle was calculated by using a quasi–one-dimensional approximation and an empirical expression, much like the procedure of Dahneke and Cheng (1979a, b). Such calculations provide valuable information concerning the factors (number of lenses, lens/nozzle geometry) that control both beam quality and particle terminal velocity. However, Liu et al.'s analysis was limited to particles located near the axis and to small particles ($D_p < 250$ nm). The authors were not able to study the loss of larger particles as a result of impact on system surfaces.

We have calculated the gas-particle flow field in an aerodynamic lens-nozzle expansion using the Fluent (Fluent, Inc., Lebanon, NH) computational fluid dynamics (CFD) package. Specifically, FLUENT4.5.2 was used and the grid was generated

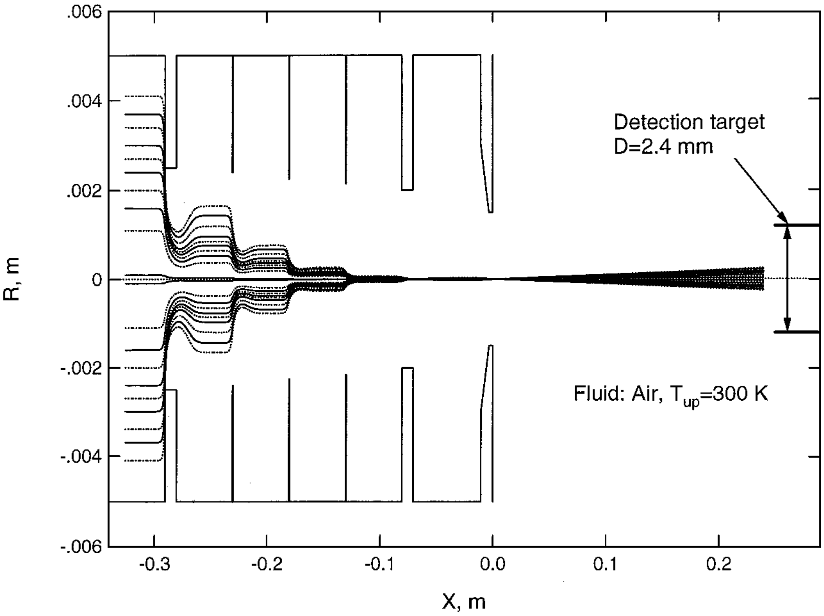

Figure 1. Schematic of aerodynamic lens system and nozzle inlet showing the calculated trajectories of 500 nm particles. $P_{\mathrm{up}} = 280$ Pa, $P_{\mathrm{down}} = 0.1$ Pa, $\mathrm{Re}_0 = 20.8$, $Q = 97.6$ scc/min, and $OD = 10$ mm. The detection target diameter is 2.4 mm, which together with its distance from the nozzle (240 mm) defines a detection angle of 0.005 rad. T_{up} is gas upstream temperature.

by GEOMESH. Fluent can simulate the full range of continuum sub-, trans-, and supersonic flows in the aerodynamic lens-nozzle inlet without major assumptions, such as constant entropy or incompressibility. The CPU time (HP9000, 450 MHz CPU) for a typical calculation of the low speed flow in a lens is about 1 h. For high speed flow in a nozzle it is about 10 h. The objective of this work is to provide a fundamental understanding of the factors that control the formation of a beam containing particles with diameters from 5 to 10,000 nm. This paper presents systematic results on the motion of particles through a single subsonic lens and on a supersonic expansion through a nozzle to vacuum. Since the isolated aerodynamic lens and the nozzle are the elementary components of an aerodynamic lens-nozzle inlet system, a fundamental understanding of these components is essential for designing the whole inlet system with the desired sampling rate and beam divergence. Detailed modeling results for an integrated aerodynamic lens-nozzle inlet system, such as that shown in Figure 1, will be presented in another paper.

SINGLE LENS SYSTEM

Figure 2 is a schematic of a single lens system with a plot of a gas streamline and a trajectory line for a 500 nm diameter particle. The figure shows that, far upstream of the lens, the selected particle follows the gas toward the lens at a radial coordinate of $R_{pi} = 4$ mm. As the gas approaches the lens, it is accelerated radially inward and one can see that the particle overshoots the gas streamlines toward the axis. Downstream of the lens, the particle moves radially outward, but only slightly, and then settles onto a streamline with a smaller radial coordinate, R_{po}. The lens is of inlet diameter ID_1, outlet diameter ID_2, and thickness L. The lens is inserted into a tube of diameter OD. Note that ID_1 and ID_2 are generally not equal, although $ID_1 = ID_2$ in Figure 2. The gas upstream pressure is 280 Pa, and the upstream gas Reynolds number, Re_0 (based on OD), is 12.5. The contraction ratio, which describes the change in the radial position of a test particle, is

$$\eta_c = \frac{R_{po}}{R_{pi}} \qquad [1]$$

NUMERICAL METHOD

The gas flow field was calculated in Fluent by assuming particle-free flow. After the gas flow field was calculated, particle trajectories were calculated by integrating the particle momentum equation. This procedure requires that particle/particle interactions be negligible and that the particles have little or no influence on gas flow. A major assumption in the gas flow field calculation is the presumption of continuum flow. The present lens and nozzle are designed to work at ~300 Pa, at which pressure the gas mean free path (λ) is on the order of 20 microns. As the gas mean free path is much smaller than the lens/nozzle dimensions ($L \sim 1$ mm with $\lambda/L \sim 0.01$), flow inside the lens-nozzle system can, in fact, be treated as a continuum flow. However, well downstream of the nozzle, where pressure is only 0.1 Pa (measured in a typical system, see Jayne et al. (2000)), and the dimension of the vacuum chamber, L, is about 100 mm,

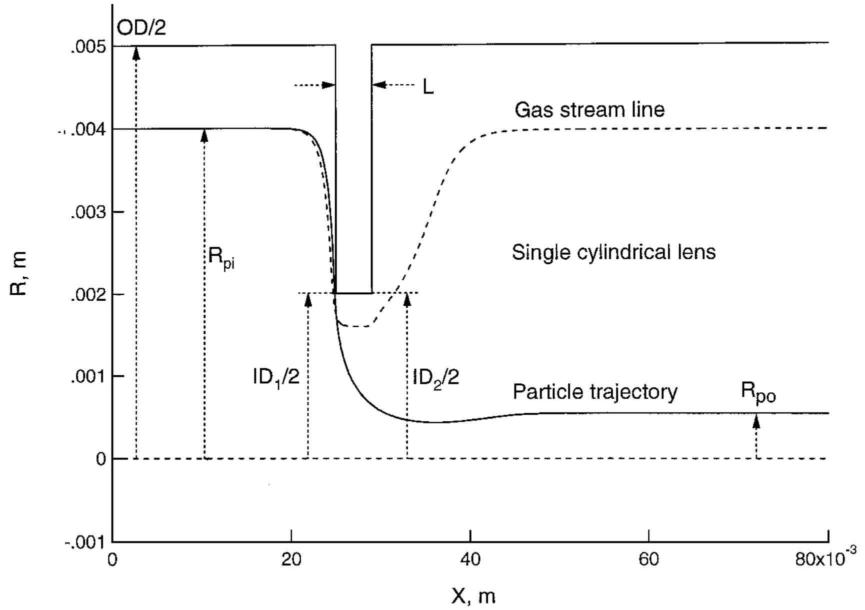

Figure 2. Schematic of a single thin cylindrical lens showing a gas streamline and the trajectory of a 500 nm particle. $Q = 60$ sec/min, $L = 4$ mm, $ID_1 = ID_2 = 2$ mm, $OD = 10$ mm, $\mathrm{Re}_0 = 12.5$, $P_{\mathrm{up}} = 280$ Pa, $R_{pi} = 4$ mm, $R_{po} = 0.5$ mm.

the flow is not of the continuum type as $\lambda/{\sim}1$. The gas flow field calculation with Fluent will not be valid under these conditions. However, the calculation shows that gas velocity reaches a maximum of about 5 mm downstream of the nozzle, at which point the pressure is about 5 Pa. Here the calculation is still valid ($\lambda = 1.2$ mm, free jet R dimension ~15 mm leading to $\lambda/L \sim 0.1$). Fortunately, the results show that events in the low pressure region have little influence on particle velocity except for particles of $D_p \leq 20$ nm (5% reduction in terminal velocity has been found for $D_p = 20$ nm particles during further expansion to lower pressure). This conclusion is supported by the good agreement between particle axial terminal velocity calculated by Fluent and experimental data down to 40 nm in diameter by Jayne et al. (2000) and Liu et al. (1995b).

Particles are assumed to be spherical throughout this work. However, it should be noted that the motion of nonspherical particles produces additional lift forces so that such particles are less well collimated (Liu et al. 1995a, b; Jayne et al. 2000). In the calculation, gravity was neglected. However, for the largest particle investigated (10 micron), it is estimated that the particle displacement due to gravity within one lens spacing (50 mm) is about 0.12 mm. This is marginally significant and provides an incentive to keep the lens spacing short if large particles are to be measured. Alternatively, one could employ an instrument that is vertically aligned. For smaller particles, the effect is entirely negligible. Other assumptions are as follows: (a) perfect gas, (b) adiabatic flow, and (c) laminar flow. The Mach number for flow in the tube and through the lens is very low, so the flow can be considered as either isothermal or adiabatic. The Mach number in the nozzle is as high as 2 and the flow there is not isothermal, but it can be considered as adiabatic. The value of the Reynolds number in both the lens and nozzle is on the order of 10, so the flow is laminar.

To ensure that results on beam contraction are independent of the numerical grid density and the geometrical parameters of the computational domain, the calculations were subjected to a series of tests. It will be shown later in the paper that the density of the computation grid (5–15 grid/mm in R and 3–15 grid/mm in X) was adequate, and the borders of the computational domain up- and downstream of an orifice were moved far away until they did not influence the flow field calculations significantly.

If the Mach number is low, as in the case of Figure 2 ($\mathrm{M}_0 \sim 0.03$), the Reynolds number alone is sufficient to characterize the gas flow field:

$$\mathrm{Re}_0 = \frac{\rho_0 V_0 OD}{\mu_0}, \tag{2}$$

$$\mathrm{M}_0 = \frac{V_0}{C_0}, \tag{3}$$

where V_0, μ_0, ρ_0, and C_0 are the average flow velocity, the gas viscosity, the gas density, and the sonic speed based on the upstream flow conditions.

The equation of motion for a particle can be written as

$$\frac{dV_p}{dt} = \frac{V - V_p}{\tau}, \tag{4}$$

where V_p is the particle velocity, V is the gas velocity, and τ is the particle relaxation time. If, as in the current case, the particle Reynolds number (defined as $|V - V_p|\rho_g D_p/\mu$) is on the order of 0.01, τ can be written as

$$\tau = \frac{\rho_p D_p{}^2 C_s}{18\mu} \qquad [5]$$

where ρ_p and D_p are particle density and diameter, respectively. C_s is a correction coefficient to Stokes' law, which is important if the particle diameter is not much larger than the gas mean free path. It can be expressed as

$$C_s = 1 + \mathrm{Kn}_p[A + Q\exp(-B/\mathrm{Kn}_p)], \qquad [6]$$

where Kn_p is the particle Knudsen number, defined as the ratio of the gas mean free path to particle diameter, and A, Q, and B are 1.21, 0.41, and 0.89, respectively (Allen and Raabe 1982). Typical values of Kn in this work were 2.2 to 4400, so particle drag is largely associated with the free molecular flow regime, for which $C_s \to A\mathrm{Kn}_p$.

Particle motion is usually characterized in terms of the Stokes number, which is defined as

$$\mathrm{St} = \frac{\tau V_c}{L_c}, \qquad [7]$$

where V_c and L_c are characteristic velocity and length scales, respectively.

Equations (5)–(7), together with the well-known expression for mean free path, yields

$$\mathrm{St} = \begin{cases} \dfrac{\mathrm{k}T}{18\mu\sqrt{2}\sigma P}\,\dfrac{V_c}{L_c}\,\rho_p D_p, & \text{free molecule regime,} \\ \dfrac{1}{18\mu}\,\dfrac{V_c}{L_c}\,\rho_p D_p^2, & \text{continuum regime,} \end{cases} \qquad [8]$$

where σ is the molecular collision cross section, P is the gas pressure, and k is the Boltzmann constant. Equation (8) clearly indicates that St in the free molecule regime is a function of gas microscopic properties (σ, μ, and P), gas velocity, lens characteristic dimension, and particle properties ($\rho_p D_p$). Therefore for a given lens system operating under constant flow conditions in the free molecule regime, the Stokes number depends on the product $\rho_p D_p$. In the continuum regime, however, the functional dependence of particle Stokes number on the particle properties goes as $\rho_p D_p{}^2$. Note that particle diameters in this paper are presented as particle aerodynamic diameter ($\rho_p D_p$ with ρ_p equal to one g/cm^3) unless specified.

RESULTS AND DISCUSSION

Particle Motion through a Single Lens

Numerical analysis of a single lens was undertaken in order to develop an understanding of effects of lens geometry and flow conditions on beam contraction. This understanding can provide general guidance for the design of a lens system. For all dimensional results, it was assumed that the fluid was air and that the upstream temperature was 300 K.

Figure 3 shows plots of particle trajectories through a single thin cylindrical lens with $ID_1 = ID_2 = 5$ mm, thickness $L = 0.5$ mm, and $OD = 10$ mm. In the single lens analysis, the upstream air pressure is 280 Pa and the flow rate, Q, is 60 sec/min. These parameters result in $\mathrm{Re}_0 = 12.5$, where Re_0 is based on the upstream quantities evaluated at $X = 0$. The top plot (Figure 3a) is for 5 nm diameter particles. It shows almost no net radial displacement of the particles because the particle inertia is so small that the particles closely followed the streamlines. The middle plot (Figure 3b) is for 500 nm diameter particles, and the particle trajectories now exhibit a strong radial contraction effect. The bottom plot (Figure 3c) is for 10,000 nm diameter particles. This plot shows that these particles have so much inertia that their trajectories are hardly influenced by the contraction and expansion of the gas flow through the lens. Another key feature in this plot is that some particles impact on the lens, leading to particle loss and a reduction in transmission efficiency. In the present analysis of a single lens, particle transmission efficiency, η_t, is defined as the particle downstream flow rate divided by the upstream flow rate. It is assumed that particles are uniformly dispersed in the air upstream of the lens

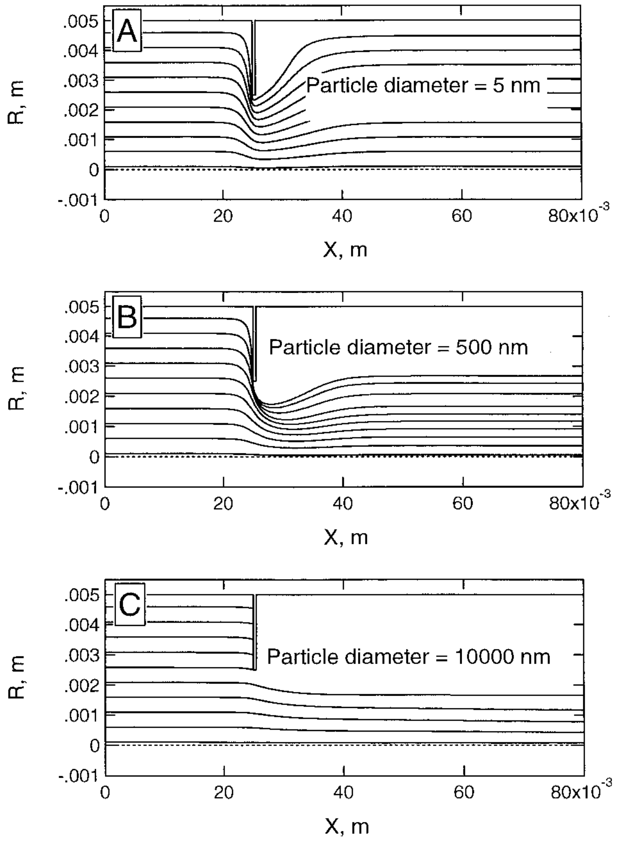

Figure 3. Particle trajectories through a single thin cylindrical lens (D_p = 5,500, 1000 nm). $L = 0.5$ mm, $ID_1 = ID_2 = 5$ mm, $OD = 10$ mm, $Q = 60$ scc/min, $\mathrm{Re}_0 = 12.5$, and $P_{\mathrm{up}} = 280$ Pa.

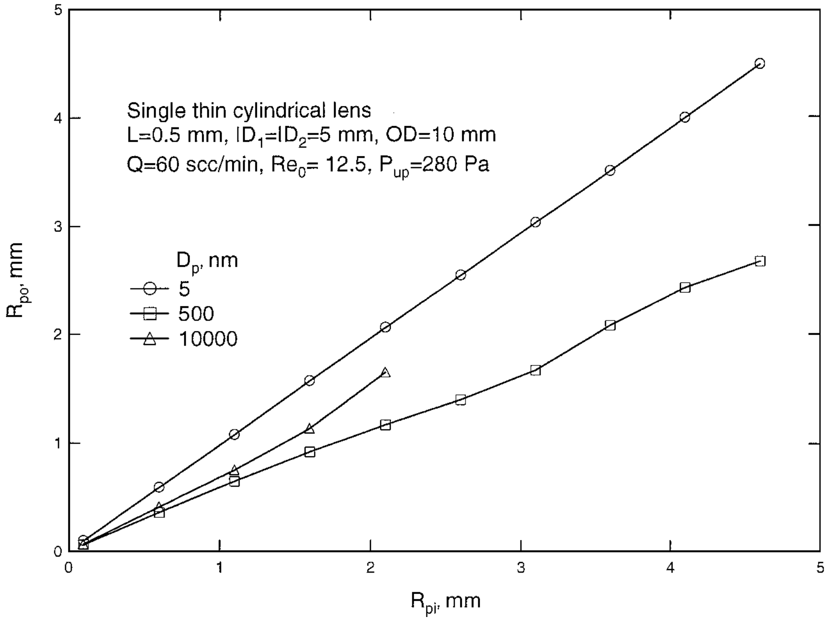

Figure 4. Particle downstream radial coordinate, R_{po}, versus upstream radial coordinate, R_{pi}, for $D_p = 5$, 500, and 10000 nm. Other parameters are the same as in Figure 3.

and that any particle that impacts on the orifice plate is lost from the flow. For a parabolic upstream velocity profile and purely ballistic particles, the transmission efficiency is given by

$$\eta_{t,b} = 2\left(\frac{ID}{OD}\right)^2\left[1 - \frac{1}{2}\left(\frac{ID}{OD}\right)^2\right]. \qquad [9]$$

This provides a lower bound for the actual transmission efficiency.

In Figure 4, the particle trajectory results from Figure 3 are plotted as downstream radial-coordinate, R_{po}, versus upstream radial-coordinate, R_{pi}. The results for $D_p = 5$ nm form a straight and nearly diagonal line, which confirms the lack of any significant radial contraction. The line for $D_p = 500$ nm is almost straight with a slope of about 0.5. This indicates that the contraction ratio, η_c, is a constant equal to 0.5. A roughly linear relationship between R_{po} and R_{pi} was also observed for $D_p =$ 10,000 nm, but with a larger slope due to higher particle inertia. The results in Figure 4 suggest that the beam contraction ratio is roughly constant. It is therefore appropriate to use the contraction ratio $\eta_c = R_{po}/R_{pi}$ at a certain R_{pi} to quantify the lens collimation effect. Throughout the present work, η_c at $R_{pi} = 1.5$ mm or $R_{pi}/OD = 0.15$ is used to represent overall lens performance. This is similar to the near axis η_c used by Liu et al. (1995a, b).

Figure 5 shows results for η_c versus particle diameter for a typical lens ($ID = 5$ mm, $OD = 10$ mm, $L = 0.5$ mm) operating at a typical condition ($P_{\mathrm{up}} = 280$ Pa, $Q = 60$ sec/min, $Re_0 = 12.5$), but at different grid densities. One can see that each curve in Figure 5a starts from η_c close to unity, because particle inertia is too small to produce a contraction, and then reaches a minimum at a certain diameter, which is referred to as the maximal collimation diameter. Finally, η_c increases for particles that are too heavy to respond to the gas contraction/expansion. This suggests that, for a given lens upstream pressure, particles of diameters around the maximal collimation diameter are efficiently displaced. Figure 5a demonstrates that double or half of the normal grid density (R-11 grid/mm, X-7 grid/mm, squares) does not significantly alter the results (maximum deviation is about 1%), but using one quarter of the normal grid density produces a noticeable deviation (6%) from the calculation with the normal grid density.

Figure 5b provides corresponding results for the transmission efficiency (η_t) versus particle diameter. The particle transmission efficiency starts at unity because there is no impact loss for small particles. At a characteristic diameter at which particles have appreciable displacement in the top plot, there is a sharp drop in the transmission efficiency due to impact loss. Finally, for sufficiently large particles, the impact loss is simply geometrical blocking, i.e., particles at $R_{pi} > ID/2$ are blocked by the lens, whereas all others are transmitted, as described by Equation (9). Similar to the results for η_c plotted in Figure 5a, Figure 5b demonstrates that double or half of the normal grid density (R-11 grid/mm, X-7 grid/mm) does not significantly alter the results for η_t (maximum deviation is about 2.5%), but one quarter of the normal grid density results in clear deviation (6%) from the calculation with the normal grid density. It should be noted that the accuracy of η_t is also influenced by the resolution in R_{pi} (currently 0.1 mm) for test particles. For instance, for the circles and squares at 10^4 nm in Figure 5b, it was found that test particles injected $R_{ip} = 2.5$ mm passed through the lens, but test particles at $R_{ip} = 2.6$ mm impacted. η_t is calculated as 0.438 based on $R_{pi} = 2.5$ mm as the maximum radius for particles

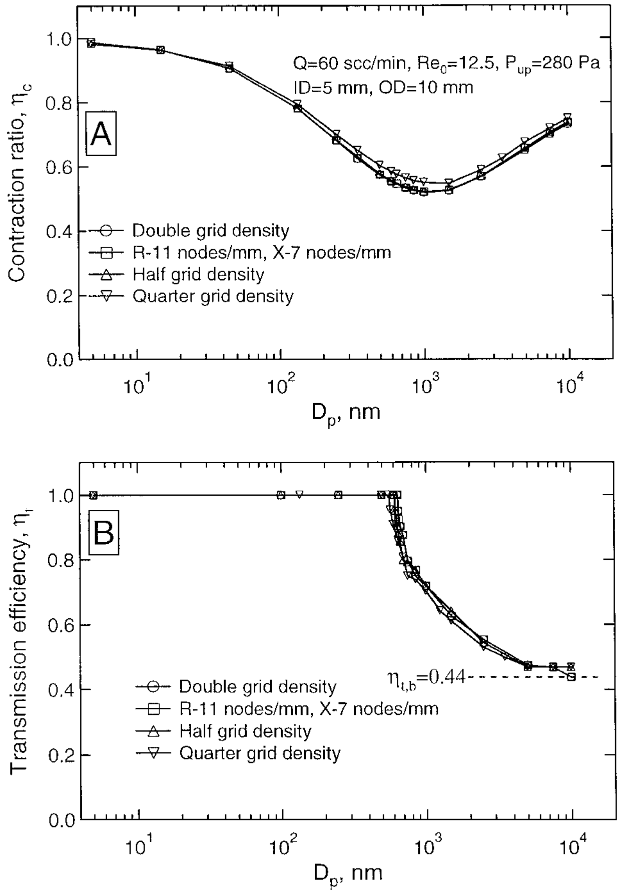

Figure 5. Particle beam contraction ratio (a) and transmission efficiency (b) versus particle diameter for a single thin cylindrical lens calculated with different grid densities. Parameters are the same as in Figure 3.

that pass through the lens. The triangles are the cases for which $R_{pi} = 2.6$ mm particles pass through the lens but $R_{pi} = 2.7$ mm particles did not; and this lead to $\eta_t = 0.468$. This introduces a maximum uncertainty of 6%, and no effort to increase the R_{pi} resolution has been attempted.

For the low speed expansion of a dilute gas-particle mixture through a lens as shown in Figure 3, the gas exhibits little compressibility so the contraction ratio (η_c) and the transmission efficiency (η_t) must be functions only of lens geometry, gas upstream Re_0 (which describes the gas flow field), and particle St (which describes the departure of the particle trajectory from the gas streamline). One would also expect that maximum contraction and significant particle impact loss would both occur at St around 1. For the case of a cylindrical lens, the relationships can be expressed as

$$\eta_c = f\left(\frac{ID}{OD}, \frac{L}{ID}, \mathrm{Re}_0, \mathrm{St}\right), \qquad [10]$$

$$\eta_t = g\left(\frac{ID}{OD}, \frac{L}{ID}, \mathrm{Re}_0, \mathrm{St}\right), \qquad [11]$$

where $ID = ID_1 = ID_2$.

To test the validity of Equations (10)–(11), η_c and η_t were calculated by changing the flow field parameters with lens dimensions fixed or changing lens dimensions with flow field parameters fixed. Re_0 and the dimensionless lens geometry (ID/OD) were kept constant in either case. Operationally, for a lens of fixed geometry, η_c and η_t were calculated by specifying a number of different upstream pressures. For each upstream pressure, a trial-and-error calculation was then undertaken to determine that value of the downstream pressure that would give the same gas mass flow rate as had been found in the base case. This is equivalent to keeping the upstream Reynolds number constant. Results of this calculation for a thin plate lens are plotted versus particle diameter in Figure 6, where upstream gas pressures were 140–340 Pa, whereas lens geometry and gas mass flow rate are unchanged ($ID = 5$ mm, $OD = 10$ mm, $L = 0.5$ mm, and $Q = 60$ scc/min, $\mathrm{Re}_0 = 12.5$). One can see that each curve in Figure 6 exhibits trends that are similar to those in Figure 5. In addition, it is observed that the maximal collimation particle size is smaller for lower upstream

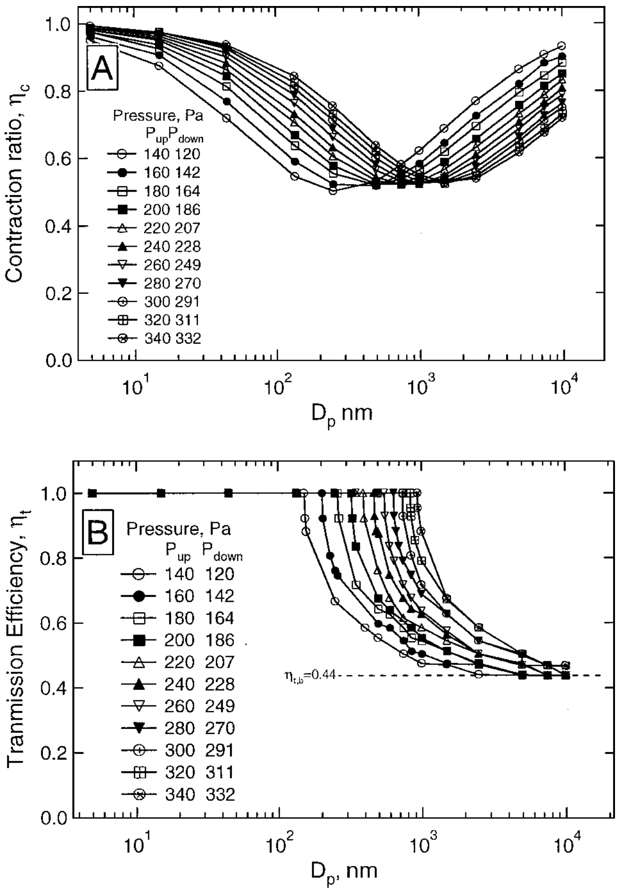

Figure 6. Particle beam contraction ratio (a) and transmission efficiency (b) versus particle diameter for a single thin orifice lens with gas upstream pressure varying from 140 Pa to 340 Pa. $\mathrm{Re}_0 = 12.5$, $ID = 5$ mm, $OD = 10$ mm, $L = 0.5$ mm, $Q = 60$ scc/min.

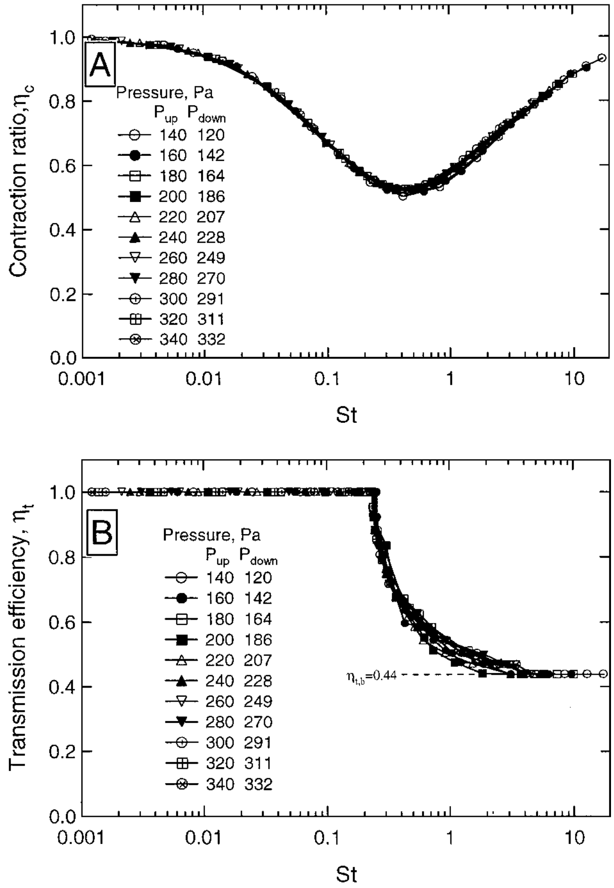

Figure 7. As in Figure 6, but plotted versus particle Stokes number. The figure shows that both the maximum beam contraction and significant particle impact loss occur at St $\cong$ 1.

pressures and the impact loss starts at a smaller diameter at lower pressures.

The data in Figure 6 are replotted in Figure 7 versus Stokes number, St, which is defined in Equation (7). Here L_c is taken as ID_1 and V_c is set equal to V_0. Figure 7 shows that all the curves in Figure 6 collapse onto 2 nearly universal curves for η_c and η_t. On the other hand, deviations from universality are larger than those due to grid density effects and R_{pi} resolution (5% and 14% versus 1% and 6% for η_c and η_t, respectively). The deviations in Figure 7 are probably due mainly to differences in the pressure drop across the lens for different upstream pressures (14% for $P_{\text{up}} = 140$ Pa and 2% for $P_{\text{up}} = 340$ Pa). As a result, particle characteristic time, τ, depends not only on the upstream pressure, but also on pressure drop. Another source of uncertainty is a lack of convergence ($\pm 2\%$) to a value Q of 60 scc/min.

In Figure 7a, it is shown that the minimum η_c occurs at St around 1, and in Figure 7b, the onset of significant impact losses also occurs at St $\cong$ 1. As expected, the results depend only on St and Re_0. A practical lens design seeks maximum particle contraction and minimum impact loss. Because of significant impact loss at St $\cong$ 1, the results suggest that it is not appropriate to operate a lens at St $\cong$ 1 unless the particles have been previously collimated. Instead, a reasonable operating condition is St $\cong$ 0.2, where there is considerable trajectory contraction but no impact loss. Figure 6 simply reflects the fact that the Stokes number in the free molecule regime (Equation (8)) is roughly proportional to $1/P^2$ when $\rho_0 V$ is held constant. In addition, since the optimum particle diameter corresponds to St $\cong$ 0.2, it is now obvious why aerodynamic lenses usually operate at a pressure of about 300 Pa for collimating particles with diameters of about 1 micron.

Equation (10) was also tested by changing the OD from 5 to 30 mm and changing the ID such that ID/OD = constant = 0.4. In this calculation, the average upstream gas velocity, V_0, was chosen in such a way that Re_0 = constant = 12.5, as shown in Figure 8. In Figure 8a, the contraction ratio is plotted versus diameter. The plot shows that the maximal collimation diameter is smaller if the device is smaller. The contraction ratio was plotted versus St in Figure 8b, where the 4 curves are seen to collapse onto 1 universal curve with minor deviations. This is another confirmation of Equation (10),

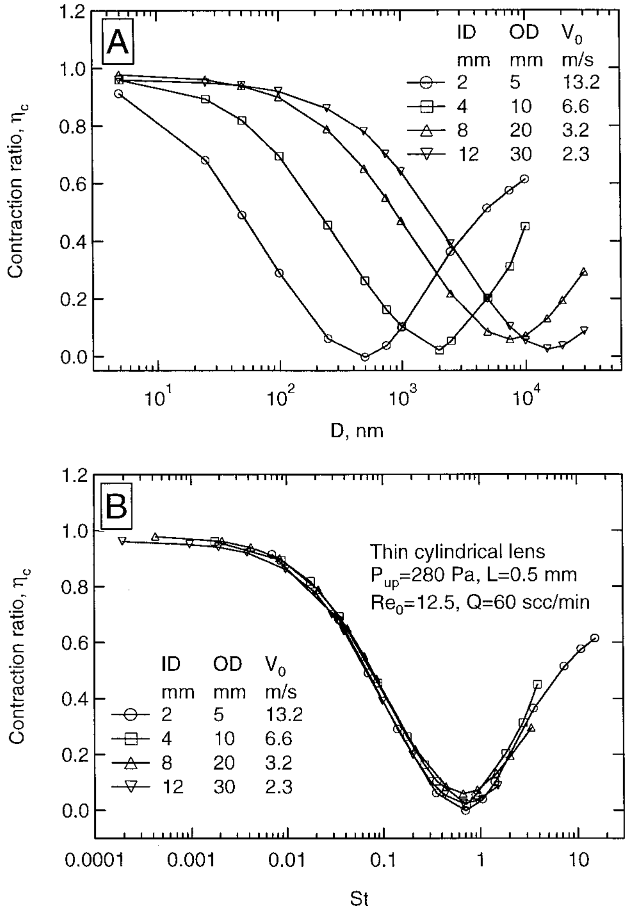

Figure 8. Particle beam contraction ratio versus particle diameter (a) and versus particle Stokes number (b) for a single thin orifice lens with ID = 2–12 mm, ID/OD = 0.4, Re_0 = 12.5, P_{up} = 280 Pa, L = 0.5 mm, Re_0 = 12.5, Q = 60 scc/min.

i.e., the particle contraction ratio is a function only of the lens dimensionless geometry, *ID*/*OD*, the Reynolds number, Re_0, and the Stokes number, St. In addition, a comparison of Figures 7 and 8 shows that the parameter *ID*/*OD* is extremely important.

Near-axis contraction ratios and transmission efficiencies at various upstream Re_0 for a single lens are plotted versus St in Figure 9 for the case of a fixed thin cylindrical lens of $OD = 10$ mm, $ID_1 = ID_2 = 4$ mm and $L = 0.5$ mm. Gas downstream pressures corresponding to each Re_0 are also included in the figure. The gas upstream pressure is fixed at 280 Pa. As in Figure 7, it is observed that the minimum values of η_c occur at St around 1; significant impact losses also occur at St $\cong$ 1. It is observed in the top plot that higher Re_0 led to a greater contraction and eventually η_c goes negative in the regime around the maximal collimation diameter, which means that particles moved across the center line. Similarly, in the bottom plot there appears to be a larger impact loss at higher Re_0. An examination of the streamlines for these same Reynolds numbers showed that the upstream contraction of the streamlines was more gradual for the lower values of Re_0 and more abrupt for the higher values. The associated changes in η_c and η_t are therefore not surprising.

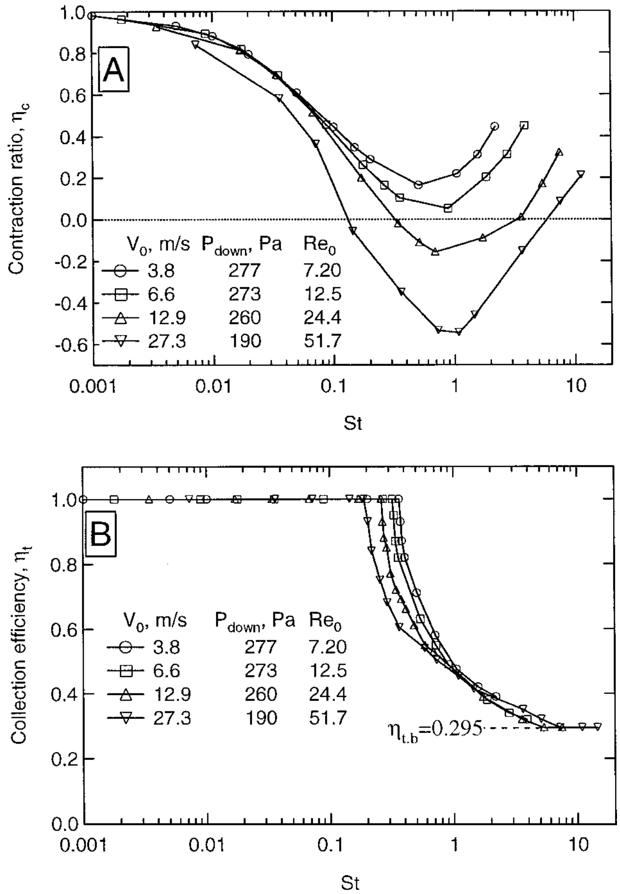

Figure 9. Particle beam contraction ratio (a) and transmission efficiency (b) versus particle Stokes number for $\mathrm{Re}_0 = 7.2$–51.7. Single thin cylindrical lens, with $L = 0.2$, $ID = 4$ mm, $OD = 10$ mm, $P_{\mathrm{up}} = 280$ Pa, $Q = 60$ scc/min.

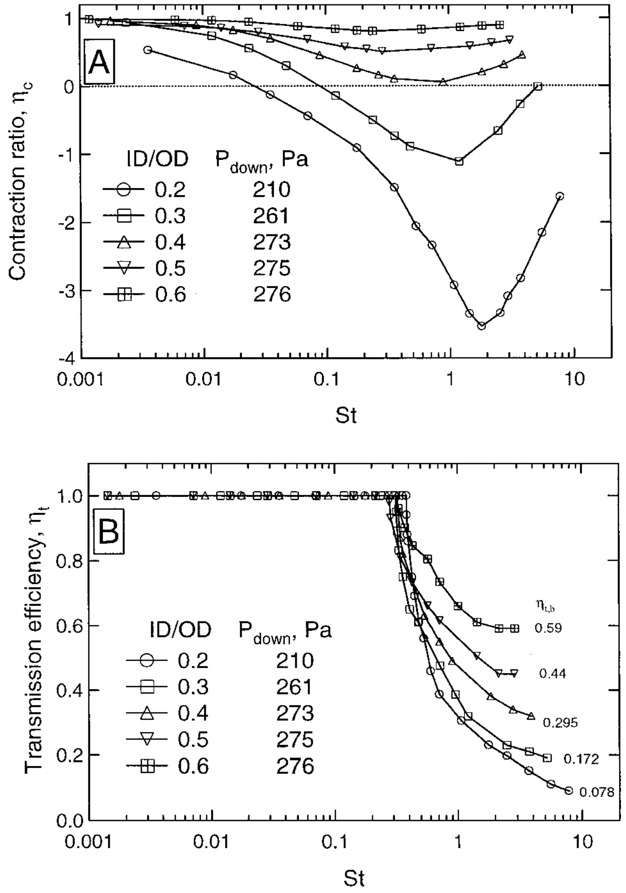

Figure 10. Particle beam contraction ratio (a) and transmission efficiency (b) versus particle Stokes number for $ID/OD = 0.2$–0.6. Single thin cylindrical lens: $L = 0.5$ mm, $OD = 10$ mm, $P_{\mathrm{up}} = 280$ Pa, $\mathrm{Re}_0 = 12.5$, $Q = 60$ scc/min.

Figure 10 shows the effect of the *ID*/*OD* ratio on contraction ratio and impact loss. Here, lens geometry and gas upstream pressure are the same as in Figures 8 and 9, except that the *ID* was varied from 2 to 6 mm. The gas flow rate was fixed at 60 sec/min, corresponding to $\mathrm{Re}_0 = 12.5$. The contraction ratio and the transmission efficiency show trends similar to those in Figures 7–8, i.e., maximum contraction and significant impact loss occur at St $\cong$ 1. In addition, the figure shows that decreasing the *ID* strongly increases the extent of beam contraction, and η_c nearly reaches -4 for $ID/OD = 0.2$. It also can be seen that there is more impact loss for a smaller *ID*/*OD* ratio due to the smaller open area. Because smaller values of *ID*/*OD* produce a more abrupt contraction of the streamlines, these results are qualitatively consistent with those in Figure 9.

The influence of the lens thickness on the particle contraction ratio is shown in Figure 11. Lens *OD* and *ID* are 10 and 4 mm, respectively, and upstream pressure and Re_0 are the same as in Figure 10. The lens thickness was increased from 0.5 to

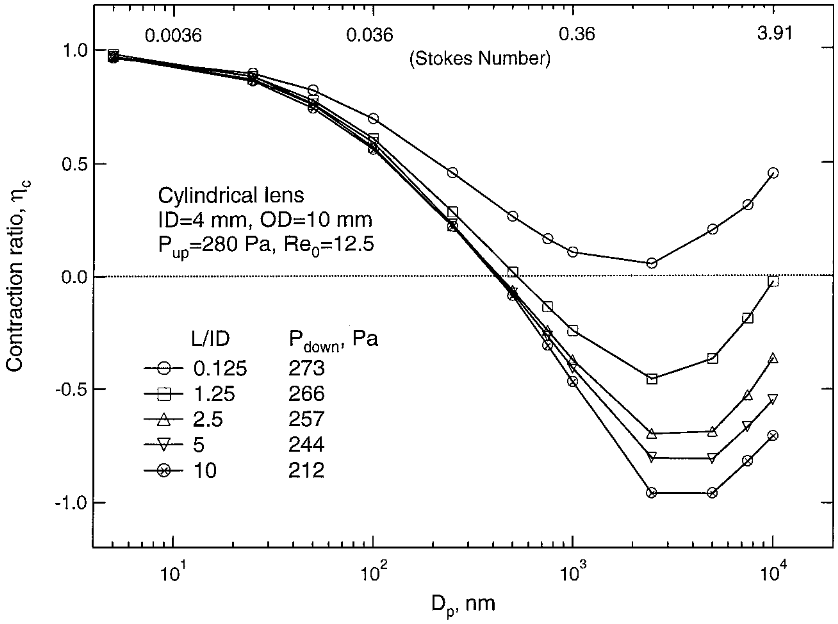

Figure 11. Particle beam contraction ratio versus particle diameter (lower axis) and Stokes number (upper axis) for $L = 0.5$–40 mm with $\mathrm{Re}_0 = 12.5$ and $Q = 60$ scc/min.

40 mm. As might be expected, the gas downstream pressures, which are shown in the figure, decrease with increasing L. Generally, it is observed that larger values of L result in stronger beam contraction. The reason for this is that a longer lens creates a larger beam contraction because the effect of downstream gas expansion is correspondingly delayed. The phenomenon is shown in Figure 12, where particle trajectories for 2.5 μm diameter particles in lenses of $L/ID = 0.125$, 1.25, and 2.5 are plotted.

Conical lenses were also studied with the expectation that they would show better transmission efficiencies than were found with cylindrical lenses. In these calculations, the lens downstream diameter, ID_2, was fixed at 4 mm, whereas the upstream diameter, ID_1, was changed from 4 to 10 mm. The lens

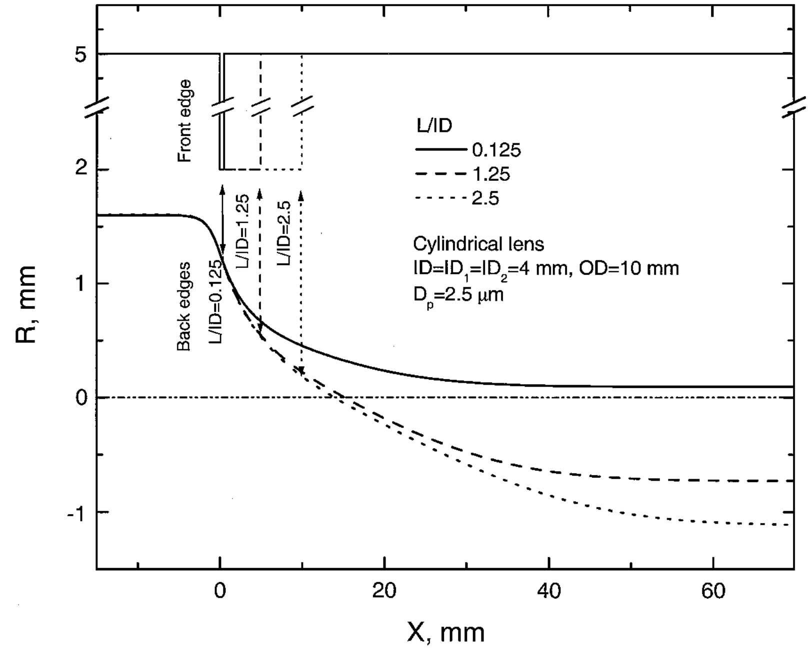

Figure 12. Particle trajectories for 2.5 μm diameter particles in lenses of $L/ID = 0.125$, 1.25, and 2.5.

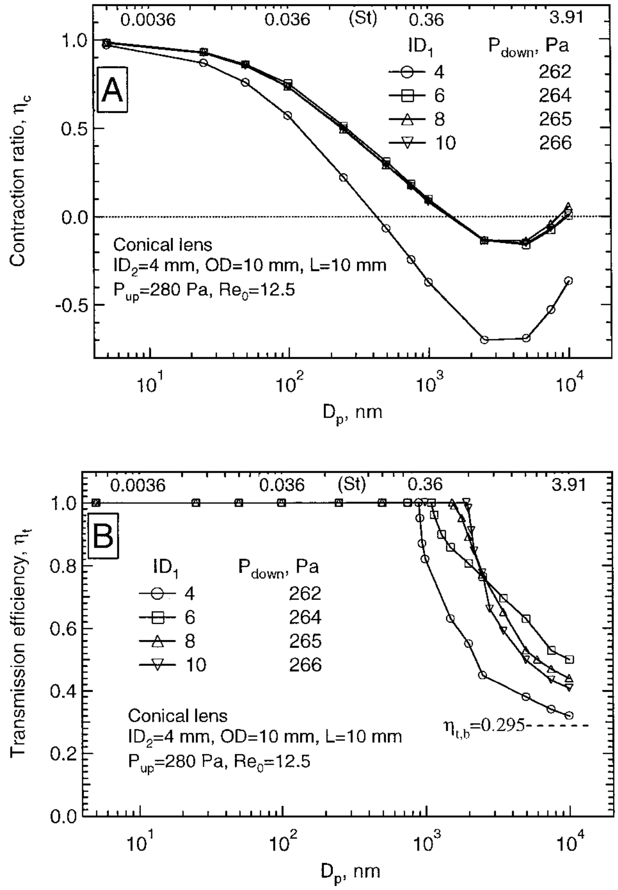

Figure 13. Particle beam contraction ratio (a) and transmission efficiency (b) versus particle diameter (lower axis) and Stokes number (upper axis) for a single conical lens with front opening diameter $ID_1 = 4$–10 mm, $ID_2 = 4$ mm, $L = 10$ mm, $\mathrm{Re}_0 = 12.5$, $Q = 60$ scc/min.

thickness was fixed at 10 mm. The results in Figure 13 show that the contraction ratio is very sensitive to small departures from the cylindrical case, but that it soon becomes independent of the upstream diameter. The transmission curves indicate that a conical lens is only modestly superior to a cylindrical lens. One can see from the figure that, by implementing a conical lens, the diameter range for 100% transmission can be extended by a factor of 2.

The results of single lens calculations indicate that the extent of contraction and impact loss are controlled by dimensionless parameters ID/OD, L/ID, Re_0, and St. Both the maximal collimation diameter and the conditions at which significant impact losses begin can be characterized by $\mathrm{St} \cong 1$.

Liu et al.'s (1995a, b) near-axis calculation also showed that η_c decreases with increasing Re_0 and increases with increasing ID/OD; however, impact losses were not analyzed. Moreover, their results showed only a monotonic decay of η_c versus St, possibly because their calculation was limited to $\mathrm{St} < 3$.

Particle Motion in a Nozzle Expansion

As discussed above, a single-stage expansion to vacuum through a conical nozzle has been used extensively to generate particle beams; previous studies have shown that both nozzle shape and upstream pressure influence beam divergence. The concept of an aerodynamic lens system was proposed by Liu et al. (1995a, b) as a technique to generate a collimated particle beam that could then be expanded to vacuum via a supersonic nozzle. Liu et al. (1995a, b) also concluded that the final nozzle geometry plays an important part in determining beam divergence. Obviously, nozzle geometry also controls particle terminal velocity, which is size dependent. This is important if particle size is to be determined by measurement of the terminal velocity. For these reasons, we have also studied flow through an isolated nozzle.

As shown in Figure 14, a 2 stage nozzle that was proposed by Liu et al. (1995a, b) has been examined. In the nozzle, the cross section available for gas flow is reduced in 2 stages: first from the tube diameter OD to d_t and, after a distance L, to the throat diameter, d_n (thickness of the throat is negligible). The pressure ratio across the nozzle is large as the pressure drops from perhaps 150 Pa to 0.1 Pa. After the throat, the gas undergoes free expansion. The quality of the resulting particle beam can be characterized by the beam divergence angle, α, which is defined as the angle between the final particle trajectory and the jet axis. The angle α is expected to be a function of gas flow parameters (upstream Reynolds number and the ratio of the up- and downstream pressures, $P_{\mathrm{up}}/P_{\mathrm{down}}$), the dimensionless geometric parameters of the nozzle, and the particle Stokes number. The reason for inclusion of $P_{\mathrm{up}}/P_{\mathrm{down}}$ here is that the gas compressibility plays a large role in determining the dynamics if this ratio is substantially larger than 1. In particular, if the ratio is about 2 (or larger), the velocity at the throat can be expected to be sonic. For a lens, $P_{\mathrm{up}}/P_{\mathrm{down}}$ is close to unity so that the compressibility effects are negligible (Mach number is <0.1); by contrast, in the nozzle expansion, $P_{\mathrm{up}}/P_{\mathrm{down}}$ is on the order of 1000 (Mach number can reach 2). In the calculations, near-axis particles at an upstream radial location of $2R_{pi}/OD = 0.1$ (R_{pi} is particle initial radial location) were chosen to characterize nozzle overall performance (as used by Liu et al. (1995a, b)), and nozzle downstream pressure was chosen as 0.1 Pa based on a typical real system (Jayne et al. 2000). Calculations were first made for a nozzle with $d_n = 3$ mm, $d_t = 6$ mm, $L = 10$ mm, and $OD = 10$ mm. Nozzle mass flow rate, Q, was 100 sec/min and the nozzle upstream pressure that matched the flow rate was 150 Pa. The particle divergence angle is plotted as squares (marked as 1:1) in Figure 14 versus particle diameter (bottom axis) or particle Stokes number (top axis). The other 2 sets of data in the figure are the cases for which the nozzle is geometrically reduced (circles marked as 0.5:1) and magnified (triangles marked as 2:1) by a factor of 2 in both the axial and radial dimensions. Obviously, the 3 nozzles are geometrically similar but have different absolute geometrical dimensions. Also in the calculations, Q/OD is maintained at a constant, because this is equivalent to

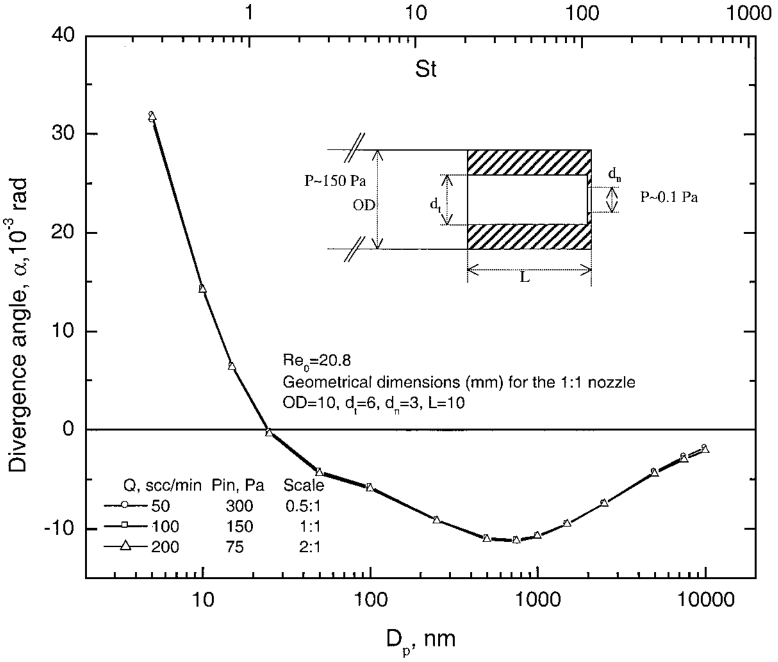

Figure 14. Particle divergence angle versus particle diameter (lower axis) and Stokes number (upper axis) for geometrically enlarged (2:1) and shrunken (0.5:1) nozzles. The geometric dimensions (mm) for 1:1 are $OD = 10$, $d_t = 6$, $d_n = 3$, $L = 10$, $\mathrm{Re}_0 = 20.8$, $Q = 100$ scc/min.

Re_0 = constant. It has been found from the calculated gas fields that Mach number profiles are similar in all 3 nozzles. Therefore flow in the 3 cases exhibits similarity. Figure 14 shows that in all 3 cases results for particle divergence angle versus particle diameter or Stokes number lie on a single curve. This is proof of the hypothesis that the nozzle dimensionless parameters (not the absolute dimensions) determine particle beam performance. Since sonic flow is expected at the throat, an appropriate velocity scale, V_c, for use in the Stokes number is the speed of sound. For convenience, we used the value of the upstream sound speed. For the Reynolds number, we used the upstream velocity as the appropriate scale, just as in the case of the lens. We also used the upstream value of τ for convenience, although this may be more difficult to justify on physical grounds. As in the lens case, we used the throat diameter as the length scale. Interestingly, it is observed in Figure 14 that the divergence angle is positive for small D_p (because smaller particles follow the gas stream), but then becomes negative for large D_p (because larger particles may cross the axis due to inertia). The beam is least divergent for those very large particles ($D_p > 5$ μm) that are too heavy to respond appreciably to the gas contraction and expansion occurring up- and downstream of the nozzle. The figure also shows that particles cross the axis at $\mathrm{St} \geq 1$.

Calculations have also been performed for a nozzle of fixed geometry but with upstream pressures varying from 75 to 600 Pa, and this results in Re_0 varying from 8.6 to 98. The Mach number profile is found to be essentially unchanged. Figure 15 shows the particle divergence angle versus particle diameter (Figure 15a) and versus particle Stokes number (Figure 15b). Figure 15a shows that higher Reynolds numbers (higher upstream pressure) result in smaller beam divergence for larger particles ($D_p >$ 1000 nm) but larger beam divergence for smaller particles. When the data were plotted versus St in the bottom plot (Figure 15b), the 4 curves were found to be nearly coincident. This suggests that Reynolds number has a minor influence on the beam divergence, whereas Stokes number has a major influence.

The effect of nozzle geometry is shown in Figure 16, where the calculated particle divergence angle for $d_t = 3$–10 mm is presented in Figure 16a as a function of particle Stokes number. Other parameters are $d_n = 3$ mm, $OD = 10$ mm, and $P_{\mathrm{down}} = 0.1$ Pa. The gas mass flow rate was 100 sec/min for all cases and upstream Reynolds number, Re_0, equals 20.8 for all cases. Gas upstream pressures matching $Q = 100$ sec/min are also included in the figure. All the curves in the figure exhibit a similar trend in that the curves start with positive values, cross the axis at St = 0.5–5 and finally become less divergent. The diamonds ($d_t = OD = 10$ mm) and the circles ($d_t = d_n = 3$ mm) represent the limiting cases of a single step thin cylindrical nozzle and a single step thick cylindrical nozzle. The common feature of the 2 cases is that the cross section for flow was decreased in 1 step (at the throat for $d_t = OD = 10$ mm case, and at the front edge of the cylinder for the $d_t = d_n = 3$ mm case). The upside down triangles ($d_t = 8$ mm) represent a case similar to the thin cylindrical nozzle, as the cross section was decreased mostly at the throat. The other 2 lines, which represent cases of changing the cross section in 2 more-or-less equal steps,

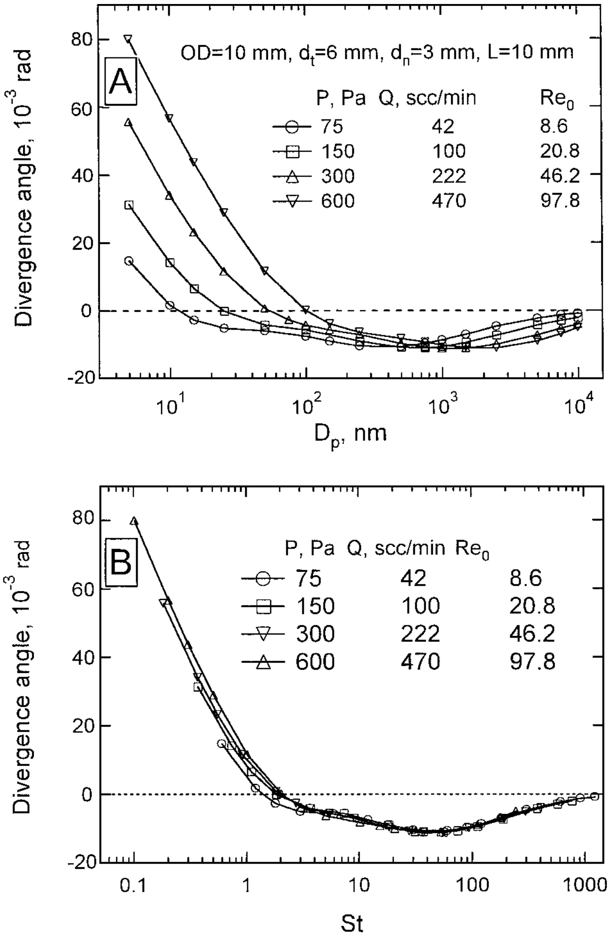

Figure 15. Particle divergence angle versus particle diameter (a) and Stokes number (b) with upstream Reynolds number varying from 8.6 to 97.8. The geometric dimensions (mm) for the nozzle are $OD = 10$, $d_t = 6$, $d_n = 3$, $L = 10$.

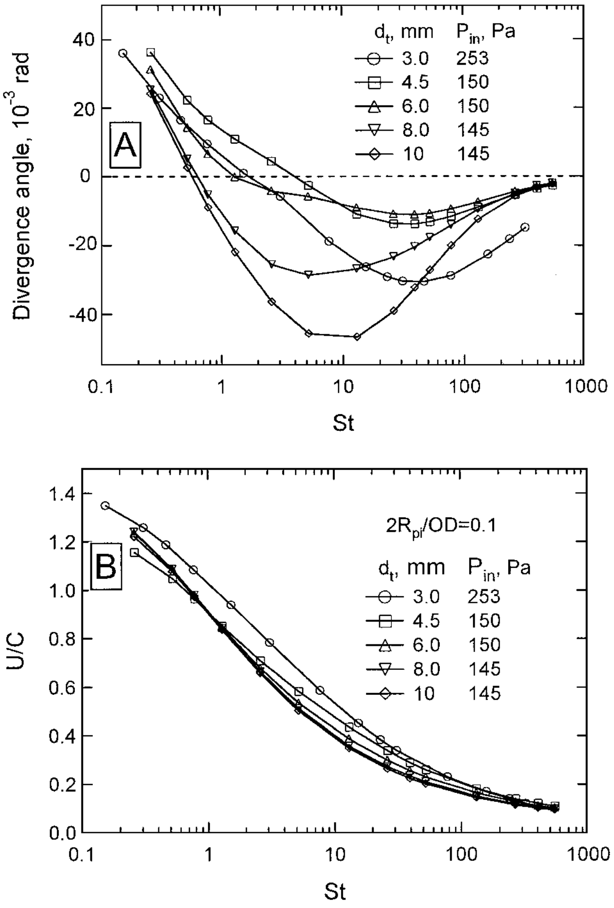

Figure 16. Particle divergence angle as a function of particle Stokes number (a) for $d_t = 3$–10 mm. (b) is particle terminal velocity (normalized by upstream sonic speed) versus Stokes number. Other parameters are $OD = 10$, $d_t = 6$, $d_n = 3$, $L = 10$, $Q = 100$ scc/min, $2R_{pi}/OD = 0.1$, $\mathrm{Re}_0 = 20.8$.

have smaller beam divergence. Among them, the right-side-up triangles ($d_t = 6$ mm, $d_t/d_n = 2$) provide the best overall performance. Additional calculations showed that further increases in the number of steps did not significantly enhance the beam performance.

Particle terminal velocity (normalized by upstream sound speed) is shown in Figure 16b versus St for the same values of the parameter d_t. The results indicate that normalized particle velocity is much less sensitive to d_t than is the beam divergence. It is interesting to note that the normalized particle velocity attains a value of 1 at $\mathrm{St} \cong 1$. Smaller particles ($\mathrm{St} < 1$) are accelerated to more than the upstream sound speed, whereas larger particles ($\mathrm{St} > 1$) attain lower velocities because of their high inertia. This result can be used to infer a particle size by measuring particle velocity. As shown in Equation (8), the particle Stokes number is proportional to $\rho_p D_p$ in the free molecule particle flow regime (which is valid for all conditions of this work), and this product is defined as particle aerodynamic diameter. This definition is different from the usual one, $\rho_p {D_p}^2$, which is valid for the continuum regime (Baron and Willeke 1993).

From a quasi-one-dimensional, semiempirical model, Liu et al. (1995a, b) calculated particle divergence angles and terminal velocities for particles up to 250 nm in diameter for $Q = 108$ sec/min for a nozzle expansion. To compare their beam divergence data with the present analysis, calculations have been performed on a nozzle of the same geometric configuration ($d_t = 6$ mm, $d_n = 3$ mm, $L = 10$ mm, $OD = 10$ mm) and with the same flow rate ($Q = 108$ sec/min) as Liu et al.'s. The results are plotted along with those of Liu et al. (1995b) in Figure 17. Figure 17b shows that the terminal velocity of particles on the axis as predicted by Fluent and by Liu et al. (1995b) are in reasonable agreement with their experimental data. However, Figure 17a shows that the Fluent model typically predicts a larger particle divergence angle than Liu et al.'s calculation. The reason for agreement of all 3 sets of data of terminal velocity in Figure 17b is probably because terminal velocity of particles on the axis is almost solely determined by gas velocity at the axis.

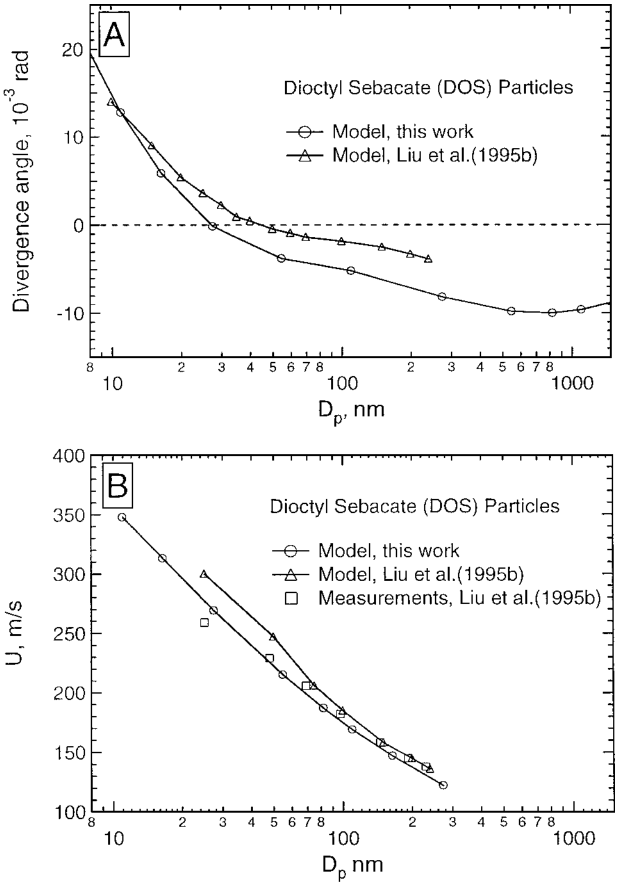

Figure 17. Particle divergence angle (a) and terminal velocity (b) versus Dioctyl Sebacate (DOS) particle geometric diameter. $OD = 10$, $d_t = 6$, $d_n = 3$, $L = 10$, $Q = 108$ scc/min, $2R_{pi}/OD = 0.1$.

In Liu et al.'s model, the gas velocity on the axis was based on a well-studied and experimentally confirmed relationship between the centerline Mach number and nozzle downstream distance. On the other hand, the discrepancy in Figure 17a probably suggests that the simple mass conservation relationship used by Liu et al. (1995b) to extract radial gas velocity has some uncertainties. These uncertainties lead to noticeable errors in beam divergence prodictions even for near-axis particles ($2R_{pi}/OD = 0.1$).

CONCLUSIONS

Particle motion for flows of gas-particle suspensions through single orifices has been investigated numerically. Both compressible and incompressible flows have been modeled.

For an incompressible flow of a gas through an orifice, the associated particles may either experience a net displacement toward the axis or they may impact on the front surface of the lens and be lost from the stream, depending on particle inertia. It was found that the extent of beam contraction and particle impact loss are controlled by the geometrical parameters *ID*/*OD* and *L*/*ID* and the dynamical parameters Re_0 and St. The maximum particle contraction is achieved at St $\cong$ 1 and significant impact loss also begins at St $\cong$ 1. The results show that a reasonable operating condition for the lens is St $\cong$ 0.2, at which condition beam contraction is close to maximum but there is no impact loss. These results can provide guidance for the sizing of each lens in a multilens system. The strategy is to (a) adjust *ID*/*OD* and Re_0 to achieve maximum value of the beam contraction; and (b) choose upstream flow parameters (velocity and upstream pressure) such that St $\cong$ 0.2 for the particle diameter of interest or operate the lens at St $\cong$ 1 if particles are already collimated.

For the final expansion through a nozzle from the lens working pressure (~150 Pa) to vacuum (0.1 Pa), it was found that particle beam divergence is a function of Re_0, nozzle geometry, and St; and, among these, the nozzle geometry and Stokes number have major impacts. It was also found that a stepped nozzle generally helps to reduce beam divergence. The calculated particle terminal velocity was shown to be in good agreement with the experimental data of Liu et al. (1995b) (Figure 17b) and separately by Jayne et al. (2000).

REFERENCES

Allen, M. D., and Raabe, O. G. (1982). Re-Evaluation of Millikan's Oil Drop Data for the Motion of Small Particle in Air, *J. Aerosol Sci.* 13:537–547.

Baron, P. A., and Willeke, K. (1993). Gas and Particle Motion. In *Aerosol Measurement*, edited by P. A. Baron and K. Willeke. John Wiley & Sons, New York, pp. 23–53.

Dahneke, B. E., and Cheng, Y. S. (1979a). Properties of Continuum Source Particle Beam. I. Calculation Methods and Results, *J. Aerosol Sci.* 10:257–274.

Dahneke, B. E., and Cheng, Y. S. (1979b). Properties of Continuum Source Particle Beam. II. Beams Generated in Capillary Expansion, *J. Aerosol Sci.* 10:363–368.

Davis, W. D. (1977). Continuous Mass Spectrometer of Airborne Particulates by Use of Surface Ionization, *Environ. Sci. Technol.* 11:587–592.

Dahneke, B. E., and Flachsbart, H. (1972). An Aerosol Beam Spectrometer, *J. Aerosol. Sci.* 3:345–349.

Estes, T. J., Vilker, V. L., and Friendlander, S. K. (1983). Characteristics of a Capillary Generated Particle Beam, *J. Colloid Interface Sci.* 93:84–94.

Henry, C. (1998). Dust in the Wind, *Anal. Chem.* 1:462A–465A.

Israel, G. W., and Friedlander, S. K. (1967). High Speed Beams of Small Particles, *J. Colloid Interface Sci.* 24:330–337.

Jayne, J. T., Leard, D. L., Zhang, X., Davidovits, P., Smith, K. A., Kolb, C. E., and Worsnop, D. R. (2000). Development of an Aerosol Mass Spectrometer for Size and Composition Analysis of Submicron Particles, *Aerosol Sci. Technol.* 33:49–70.

Johnston, M. V., and Wexler, A. S. (1995). Mass Spectrometry of Individual Aerosol Particles, *Anal. Chem.* 67:721A–726A.

Kantrowitz, A., and Grey, J. (1951). A High Intensity Source of the Molecular Beam, *Review of Scientific Instruments* 22:328–332.

Kievit, O., Weiss, M., Verheijet, P. J. T., Marijnissen, J. C. M., and Scarlett, B. (1996). The On-Line Chemical Analysis of Single Particles Using Aerosol Beams and Time of Flight Mass Spectrometer, *Chem. Eng. Comm.* 151:79–100.

Liu, P., Ziemann, P. L., Kittelson, D. B., and McMurry, P. H. (1995a). Generating Particle Beams of Controlled Dimensions and Divergence: I. Theory of Particle Motion in Aerodynamic Lenses and Nozzle Expansions, *Aerosol Sci. Technol.* 22:293–313.

Liu, P., Ziemann, P. L., Kittelson, D. B., and McMurry, P. H. (1995b). Generating Particle Beams of Controlled Dimensions and Divergence: II. Experimental

Evaluation of Particle Motion in Aerodynamic Lenses and Nozzle Expansions, *Aerosol Sci. Technol.* 22:314–324.

Mallina, R. V., Wexler, A. S., and Johnston, M. V. (1999). High Speed Particle Beam Generation: Simple Focusing Mechanisms, *J. Aerosol Sci.* 30:719–738.

Mallina, R. V., Wexler, A. S., Rhoads, K. P., and Johnston, M. V. (2000). High Speed Particle Beam Generation: A Dynamic Focusing Mechanism for Selecting Ultrafine Particles, *Aerosol Sci. Technol.* 33:87–104.

Murphy, D. M., and Thomson, D. S. (1995). Laser Ionization Mass Spectrometry of Single Aerosol Particles, *Aerosol Sci. Technol.* 22:237–249.

Murphy, W. K., and Sears, G. W. (1964). Production of Particle Beams, *J. Appl. Phys.* 85:1986–1987.

Noble, C. A., and Prather, K. A. (1996). Real-Time Measurement of Correlated Size and Composition Profiles of Individual Atmospheric Aerosol Particles, *Environ. Sci. Technol.* 30:2667–2680.

Rao, N. P., Navascues, J., and Mora, J. F. (1993). Aerodynamic Focusing of Particles in Viscous Jets, *J. Aerosol Sci.* 24:879–892.

Shreiner, J., Voigt, C., Mauersberger, K., McMurry, P., and Ziemann, P. (1998). Aerodynamic Lens System for Producing Particle Beams at Stratospheric Pressures, *Aerosol Sci. Technol.* 29:50–56.

Shreiner, J., Schild, U., Voigt, C., and Mauersberger, K. (1999). Focusing of Aerosol into a Beam at Pressures from 10 to 150 Torr, *Aerosol Sci. Technol.* 31:373–382.

Thomson, D. S., Middlebrook, A. M., and Murphy, D. M. (1997). Threshold for Laser Induced Ion Formation from Aerosols in a Vacuum Using Ultraviolet and Vacuum Ultraviolet Laser Wavelengths, *Aerosol Sci. Technol.* 26:544–559.

Tobias, H. J., Kooima, P. M., Dochery, K. S., and Ziemann, P. J. (2000). Real-Time Chemical Analysis of Organic Aerosols Using a Thermal Desorption Particle Beam Mass Spectrometer, *Aerosol Sci. Technol.* 33:170–190.